# Capillary-driven horseshoe vortex forming around a micro-pillar

K. Ozawa, H. Nakamura, K. Shimamura, G.F. Dietze, H.N. Yoshikawa, Farzam Zoueshtiagh, K. Kurose, L. Mu, I. Ueno

# Capillary-driven horseshoe vortex forming around a micro-pillar

K. Ozawa[a], H. Nakamura[a], K. Shimamura[a], G. F. Dietze[b], H. N. Yoshikawa[c], F. Zoueshtiagh[d], K. Kurose[e], L. Mu[f], I. Ueno[e,*]

[a]*Division of Mechanical Engineering, School of Science and Technology, Tokyo University of Science, 278-8510, Chiba, Japan*
[b]*Université Paris-Saclay, CNRS, FAST, 91405, Orsay, France.*
[c]*Université Côte d'Azur, CNRS, Institut de Physique de Nice, 06100 Nice, France*
[d]*Univ. Lille, CNRS, Centrale Lille, Univ. Polytechnique Hauts-de-France, UMR 8520 - IEMN, F-59000 Lille, France*
[e]*Department of Mechanical Engineering, Faculty of Science and Technology, Tokyo University of Science, Chiba 278-8510, Japan*
[f]*Key laboratory of Ocean Energy Utilization and Energy Conservation of Ministry of Education, School of Energy and Power Engineering, Dalian University of Technology, 116024 Dalian, China*

## Abstract

*Hypothesis*: Horseshoe vortices are known to emerge around large-scale obstacles, such as bridge pillars, due to an inertia-driven adverse pressure gradient forming on the upstream-side of the obstacle. We contend that a similar flow structure can arise in thin-film Stokes flow around micro-obstacles, such as used in textured surfaces to improve wettability. This could be exploited to enhance mixing in microfluidic devices, typically limited to creeping-flow regimes.

*Experiments*: Numerical simulations based on the Navier-Stokes equations are carried out to elucidate the flow structure associated with the wetting dynamics of a liquid film spreading around a 50 µm diameter micro-pillar. The employed multiphase solver, which is based on the volume of fluid method, accurately reproduces the wetting dynamics observed in current and previous (Mu et al.,

*Corresponding author
*Email address:* ich@rs.tus.ac.jp (I. Ueno)

Langmuir, 2019) experiments.

*Findings*: The flow structure within the liquid meniscus forming at the foot of the micro-pillar evinces a horseshoe vortex wrapping around the obstacle, notwithstanding that the Reynolds number in our system is extremely low. Here, the adverse pressure gradient driving flow reversal near the bounding wall is caused by capillarity instead of inertia. The horseshoe vortex is entangled with other vortical structures, leading to an intricate flow system with high-potential mixing capabilities.

*Keywords:* horseshoe vortex, wetting, meniscus, capillarity, micropillar

## 1. Introduction

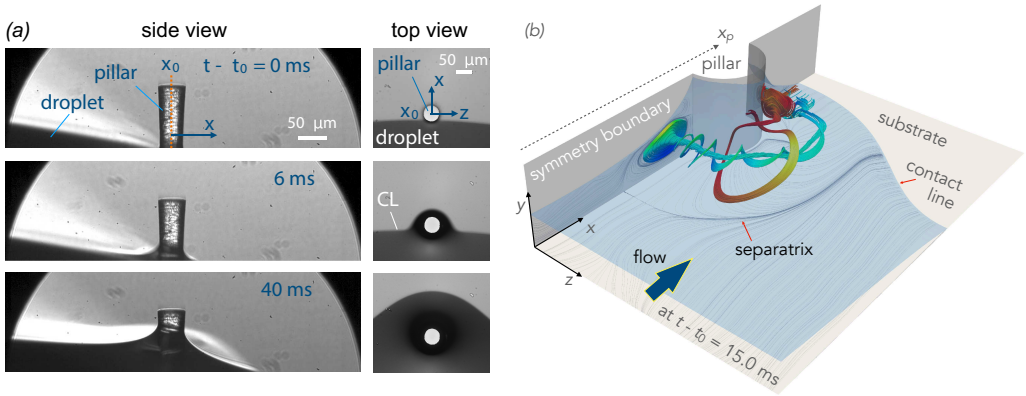


Figure 1: Horseshoe vortex (HSV) forming around a cylindrical micro-pillar (diameter $d_p$=50 µm, static contact angle $\theta_0$=20°) engulfed by a liquid film spreading on a smooth substrate ($\theta_0$=5°). The working liquid is silicone oil (dimethylpolysiloxane, KF-96L-2cs, Shin Etsu Chemical Co. Ltd.), with $\rho$=873 kg/m$^3$, $\nu$=2 mm$^2$/s, and $\sigma$=18.3 mN/m at $T$=25 °C. *(a)* Experiment performed under isothermal conditions at $T$=24.5 °C using the setup of [1]. The time of first contact between droplet and pillar is $t$=$t_0$. *(b)* Numerical simulation showing the internal flow structure of the liquid meniscus. The pillar is positioned at $x_p$=150 $\mu$m. Streamlines colored in blue, red, and black highlight the HSV, a second vortex forming in the wake of the pillar, and the flow within the planes $z$=0 and $y$=0.1 $\mu$m.

Microfluidics bears a vast potential for industrial applications [2], such as drug

mixing and dispensing [3], blood sampling [4] and analysis [5], 3D bioprinting of viable cells [6], or surface cleaning by acoustic waves [7]. At such a small scale, the flow is usually laminar and inertia is negligible. Therefore, generating sufficient mixing remains a challenge for engineering applications. Different techniques, either active or passive, have been proposed to mitigate this limitation [8, 9]. Passive techniques rely on modifying the channel geometry [10], exploiting interfacial instabilities in two-phase flows [11], or generating soft-wall turbulence through the use of compliant materials [12]. In the present work, we show via direct numerical simulations that immersing a simple cylindrical micro-pillar into a liquid film spreading on an otherwise smooth substrate allows to generate a complex and extended system of vortices around it. In particular, we uncover the existence of a horseshoe vortex, which is similar to vortices forming around large-scale obstacles such as bridge pillars [13], but caused by an entirely different mechanism, driven by capillarity and not by inertia. We find that the adverse pressure gradient causing flow reversal upstream of the micro-pillar results from an intricate competition between variations in streamwise and transverse curvature of the liquid-gas interface.

The configuration studied here is of interest in the context of dynamic wetting [14, 15]. In recent experimental studies, it was demonstrated that a tenfold increase in contact line velocity can be achieved by simply placing individual wettable micro-obstacles (e.g. beads or pillars) on the pathway of a liquid drop spreading on a silicon wafer [1, 16, 17]. Figure 1a represents a typical such experiment, which we have performed under isothermal conditions at $T$=24.5 °C using the same setup and procedure as [17]. Here, a drop of silicone oil (dimethylpolysiloxane, KF-96L-2cs, Shin Etsu Chemical Co. Ltd., with density $\rho$=873 kg/m$^3$, kinematic viscosity $\nu$=2 cSt, and surface tension $\sigma$=18.3 mN at $T$=25 °C) spreads toward a cylindrical micro-pillar (static contact angle $\theta_0$=20°) of diameter $d_p$=50 µm placed on a silicon

wafer ($\theta_0$=5°). After first contact between the advancing contact line of the drop and the pillar ($t$=$t_0$ in figure 1a), the liquid is soaked up toward the obstacle, due to the strongly curved liquid meniscus forming around its foot ($t$-$t_0$=6 ms to $t$-$t_0$=40 ms in figure 1a). This so-called *meniscus pump* sustains a rapid rise of the liquid along the low energy surface of the pillar, reducing viscous drag within the upstream liquid film and increasing the slope of the spreading front downstream of the particle. Both these effects contribute to accelerating the spreading rate [18].

In the current manuscript, we employ numerical simulation based on the full Navier-Stokes equations (see [19] for numerical details) to unveil the internal flow structures developing within the liquid meniscus during film-pillar interaction (figure 1b). We focus on a pillar of diameter $d_\mathrm{p}$=50 $\mu$m and use liquid properties and surface wettabilities according to the above-described experiments (see caption of figure 1 for all parameters). For this system, the Bond number Bo=$\rho g d_\mathrm{p}^2/\sigma \sim 10^{-3}$ and the Weber number We=$\rho U_0^2 d_\mathrm{p}/\sigma \sim 10^{-9}$ are both very low. Therefore, pressure variations due to surface tension entirely dominate those induced by gravity and inertia. Here, we have used the contact line velocity $U_0 \sim 10^{-4}$ m s$^{-1}$ prior to first contact as velocity scale, which yields a Reynolds number of Re=$U_0 d_\mathrm{p}/\nu \sim 10^{-3}$.

Despite that Re is very low, we observe the formation of a horseshoe vortex (HSV) around the micro-pillar, as shown in figure 1b, which represents a snapshot from our simulation. In this figure, different flow structures within the liquid are highlighted via groups of colored streamlines and the liquid-gas interface is visualized in transparent blue. We distinguish a main HSV wrapping around the pillar in the direction of the flow (blue color palette), which is entangled with a second vortex forming in the wake of the pillar (red color palette). This complex system of vortices suggests that micro-pillars may be used to enhance mixing, in addition to their benefits in contact line acceleration [1].

In light of the state of the art on horseshoe vortices, it is surprising to achieve

such flow complexity in our microfluidic system. HSV are known to form around large- and medium-scale obstacles placed into wall-bounded flows [13]. In civil engineering, they can cause erosion and structural damage to bridge pillars ($d_\mathrm{p} \sim 1$ m) in river beds [20]. HSV have also been observed at smaller scales, e.g. in pin fin arrays ($d_\mathrm{p} \sim 1$ mm) used in high-temperature heat exchangers [21]. In both examples, the adverse pressure gradient driving the HSV results from a conversion of kinetic energy, $\rho U_\infty^2/2$ (where $U_\infty$ is the free-stream velocity), into static pressure $p$, as the flow decelerates toward the pillar. When the Reynolds number $\mathrm{Re}_\infty = U_\infty d_p/\nu$ exceeds a threshold value $\mathrm{Re}_\infty^\mathrm{crit}$, the adverse pressure gradient overcomes viscous drag, leading to flow reversal near the wall upstream of the obstacle. Although this threshold $\mathrm{Re}^\mathrm{crit}$ (and the complexity of the vortex system forming around the pillar) varies greatly with obstacle geometry [22–25], there is consensus in the literature that $\mathrm{Re}^\mathrm{crit} > 1$. Thus, flow inertia is a necessary ingredient at these scales. By contrast, the HSV forming in our virtually inertialess micro-system must be caused by an entirely different mechanism. We will demonstrate here that surface tension instead of inertia acts as the driving mechanism in our case.

## 2. Simulation setup and numerical methods

The system represented in figure 1 was simulated with the finite-volume solver `interFoam` [26], which is part of the computational fluid dynamics software `OpenFOAM` (version 5.0). This solver relies on the VOF (Volume of Fluid) and CSF (Continuum Surface Force) methods [27, 28] to account for the multiphase nature of the flow.

In our simulation, we have assumed Newtonian fluids and used fluid properties and surface wettabilities according to the experiment in figure 1a. For the liquid (subscript $L$), we set $\rho_L = 873\ \mathrm{kg/m^3}$, $\nu_L = 2.0\times10^{-6}\ \mathrm{m^2/s}$, and $\sigma = 1.83\times10^{-2}\ \mathrm{N/m}$. For the ambient air (subscript $G$ for gas), we set $\rho_G = 1\ \mathrm{kg/m^3}$ and $\nu_G = 1.48\times10^{-5}$

$m^2/s$. For the static contact angle $\theta_0$, we use $\theta_0$=5° on the substrate, and $\theta_0$=20° on the pillar.

The dimensions of the computational domain and the number of grid cells per dimension are $(L_x, L_y, L_z)$ [$\mu$m] = (300, 80, 300) and $(N_x, N_y, N_z)$ = (150, 40, 150), respectively. The grid independence of our results has been checked by performing the same simulation with twice coarser spatial and temporal resolutions.

The pillar, of diameter $d_\mathrm{p}$=50 $\mu$m, is placed at the center of the domain ($x_\mathrm{p}$ = 150 $\mu$m, $z_\mathrm{p}$ = 0). We exploit the symmetry of the system with respect to the $x$-$y$ plane and represent only half of the pillar. Thus, we impose symmetry boundary conditions at the left ($z$ = 0), top ($y = L_y$), and right ($z = L_z$) boundaries of the domain. At the material surfaces of the substrate ($y$ = 0) and the pillar ($z^2 + (x - x_\mathrm{p})^2 = d_\mathrm{p}^2/4$), wall adherence and no-penetration conditions are imposed.

The liquid flows into the computational domain through an inlet channel of height $h_\mathrm{inlet}$=20 $\mu$m located at the upstream boundary ($x$=0), where we impose the pressure $p(x = 0, y, t)$=$P_\mathrm{inlet}$ = 0, and a plug-profile for the $x$-velocity $u(x = 0, y, t)$=$U_\mathrm{inlet}$=$3 \times 10^{-4}$ m/s. This value is deduced from the spreading rate in the experiments of [1].

Using the `interFoam` solver, we numerically solve the continuity and Navier-Stokes equations for an incompressible single fluid with effective density $\bar{\rho}$ and dynamic viscosity $\bar{\mu}$:

$$\boldsymbol{\nabla} \cdot \mathbf{U} = 0, \tag{1}$$

$$\frac{\partial(\bar{\rho}\mathbf{U})}{\partial t} + \boldsymbol{\nabla} \cdot (\bar{\rho}\mathbf{U}\mathbf{U}) = -\boldsymbol{\nabla} p + \boldsymbol{\nabla} \cdot \boldsymbol{\tau} + \bar{\rho}\mathbf{g} + \mathbf{F}_\mathrm{SV}, \tag{2}$$

where $\mathbf{U}$ and $p$ denote the fluid velocity vector and pressure, and $\boldsymbol{\tau}$ designates the viscous stress tensor $\boldsymbol{\tau} = \bar{\mu}(\nabla\mathbf{U} + \nabla\mathbf{U}^\mathrm{T})$.

The effective properties of the single fluid are formulated as a weighted average

of the pure-phase properties in terms of the liquid volume fraction $\alpha$:

$$\bar{\rho} = \alpha\,\rho_{\mathrm{L}} + (1-\alpha)\,\rho_{\mathrm{G}}, \quad \bar{\mu} = \alpha\,\mu_{\mathrm{L}} + (1-\alpha)\,\mu_{\mathrm{G}}. \tag{3}$$

The volume fraction $\alpha$ takes values of unity or zero when a given cell is occupied entirely by liquid or gas, and an intermediate value when a cell contains the liquid-gas interface. A rough estimate of the liquid-gas interface is given by the isosurface $\alpha$=0.5.

The field of the volume fraction $\alpha$ is obtained by solving the advection equation:

$$\frac{\partial \alpha}{\partial t} + \boldsymbol{\nabla}\cdot(\alpha\mathbf{U}) + \boldsymbol{\nabla}\cdot(\mathbf{U}_{\mathrm{c}}\,\alpha\,(1-\alpha)) = 0, \tag{4}$$

where $\mathbf{U}_{\mathrm{c}}$ is an ad hoc compression velocity used to counteract numerical diffusion [29], which is oriented in the direction of the unit normal vector $\mathbf{n}$ to the liquid-gas interface (pointing into the gas phase):

$$\mathbf{U}_{\mathrm{c}} = \|\mathbf{U}\|\,\mathbf{n}, \quad \mathbf{n} = -\frac{\nabla\alpha}{\|\nabla\alpha\|}. \tag{5}$$

Numerical diffusion can cause flotsam in multiphase computations [30]. This approach, designated as algebraic VOF approach, has the advantage of being generally applicable to unstructured meshes. Although it is less precise than other VOF-based methods, such as piecewise linear interface calculation [31] (PLIC) or coupled Level-Set/VOF [32], it has been shown to give reasonable predictions for different capillary-driven flows, in comparison with said methods [26, 29], and with experiments [33].

The effect of surface tension is accounted for via the CSF method, i.e. through the source term $\mathbf{F}_{\mathrm{SV}}$ in the momentum equation (2). This term is computed via:

$$\mathbf{F}_{\mathrm{SV}} = \sigma\kappa\mathbf{n}, \quad \kappa = \nabla\cdot\mathbf{n}, \tag{6}$$

where $\kappa$ denotes the curvature of the liquid-gas interface, which are approximated based on the volume fraction $\alpha$.

The dynamic contact angle $\theta$ of the liquid-gas interface with the solid boundaries (substrate and pillar) is imposed via the relation [29]:

$$\theta = \theta_0 + (\theta_a - \theta_r) \tanh\left(u_{\mathrm{CL}}/u_\theta\right), \tag{7}$$

which is hard-coded in `interFoam` via the boundary condition type `dynamicAlphaContactAngle` [34, 35]. Here, $\theta_0$ denotes the static contact angle, and $\theta_a$, $\theta_r$, and $u_\theta$ are adjustable parameters allowing to control the variation of the dynamic part in Eq. (7) as a function of the contact line velocity $u_{\mathrm{CL}}$ (which is approximated by the tangential fluid velocity in the wall-adjacent cells).

In our current simulation, we have identified the values of $\theta_a$, $\theta_r$, and $u_\theta$, such as to recover the appropriate spreading regime for a two-dimensional drop spreading on a plane wall, i.e. $x \propto t^{1/7}$[36], for our two liquid/solid pairings, i.e. oil/substrate and oil/pillar. We have previously applied this approach in [18], where the same liquid/solid system was simulated, only that a spherical micro-particle was used instead of a micro-pillar. In figure 5 of that reference, it was shown that the simulated contact line progressed as $x \propto t^{1/7}$ prior to contact with the micro-particle. The exact values for the adjustable parameters used in our simulation are $\theta_a$=10°, $\theta_r$=1°, and $u_\theta$=1.2 m/s for the substrate and $\theta_a$=30°, $\theta_r$=10°, and $u_\theta$=1.2 m/s for the pillar.

In equation 7, the effect of the liquid properties, $\mu_L$ and $\sigma$, is accounted for by manually adjusting $\theta_a$, $\theta_r$, and $u_\theta$ to our liquid/solid pairings, unlike the well-known Cox-Voinov relation [37], where the effect is taken into account explicitly via the capillary number $\mathrm{Ca}_{\mathrm{CL}}$=$u_{\mathrm{CL}}\mu_L/\sigma$. Nonetheless, simulations of contact line problems with the `interFoam` solver based on equation (7) have shown good agreement with experiments in the case of drop impact and spreading [34], and, as stated above, our simulations recover the $x \propto t^{1/7}$ spreading regime on flat surfaces. Also, our numerical prediction of the meniscus rise along the pillar is in good agreement with our experiment from figure 1a, as will be discussed w.r.t. figure

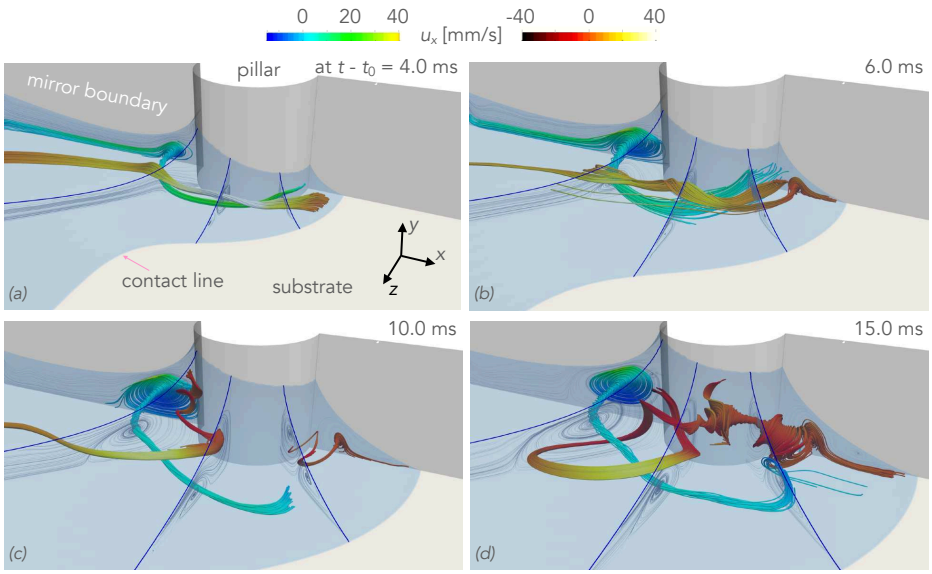


Figure 2: Time evolution of the HSV system forming around the micro-pillar. Parameters according to figure 1b. Different color palettes highlight two intertwined vortices: the HSV originating upstream of the pillar (blue/green) and a wake vortex (WV) emanating from downstream of the pillar (red/yellow). *(a)* Emergence of the HSV. *(b)* Emergence of the WV. *(c,d)* Disconnection and then re-connection of the WV.

3a, where we have produced a direct comparison.

Details of the numerical procedure for solving equations (1), (2), and (4), with the `interFoam` solver are provided in references [26, 29]. We mention here only the salient features. Spatial discretization is realized via finite volumes, using the upwind scheme for convective terms and linear interpolation for diffusional terms. Time discretization is realized via the explicit Euler scheme, and we use an adaptive time step $\Delta t$ with $\Delta t \leq 1\,\mu$s. The PISO algorithm is used to solve the momentum equations (2), while enforcing continuity (1), and the MULES approach is used to solve the volume fraction advection equation (4). The dynamic contact angle according to (7) is imposed by setting the unit normal of the liquid-gas interface (5) via a boundary condition on $\nabla\alpha$ [29].

## 3. Results

Figure 2 represents the time evolution (from panel 2a to panel 2d) of the flow structure within the liquid meniscus forming around the micro-pillar, as the silicone oil film spreads around it. We have highlighted streamlines that belong to the two principal vortical structures organizing around the pillar: the HSV (blue/green color palette), which emanates from the upstream side of the pillar, and a wake vortex (WV) forming in the wake of the pillar (red/yellow color palette). Additional streamlines based on the projected velocity field within three representative radial sections are also shown. These allow to better understand how the HSV and WV are situated around the micro-pillar.

Figure 2a corresponds to an early time, just after the liquid has engulfed and wetted the entire pillar circumference. It captures the emergence of the HSV, which wraps around the pillar in the direction of the flow. Figure 2b corresponds to a slightly later time, when the WV (red/yellow streamlines) has started to form. Although this vortex occurs in the wake of the pillar, it extends quite far upstream. As time progresses (figures 2b, 2c, and 2d), the HSV and WV become increasingly entangled, forming a complex three-dimensional structure. During this process, the WV splits into two portions (figure 2c), which subsequently reconnect (figure 2d). At long times, a swirling flow structure is established (figure 2d). Based on the streamlines drawn within the three radial cross sections, we conclude that the HSV and WV have opposite senses of rotation, as they are adjacent to one another (figure 2c).

The HSV represented in figures 1b and 2 originates within the symmetry plane ($z$=0), during the rise of the liquid meniscus along the upstream side of the pillar. Figure 3a shows the time evolution of the meniscus profile $h(x)$ in this region, following initial contact between the liquid and the pillar at $t$=$t_0$. Symbols in the same figure represent corresponding experimental profiles obtained by processing

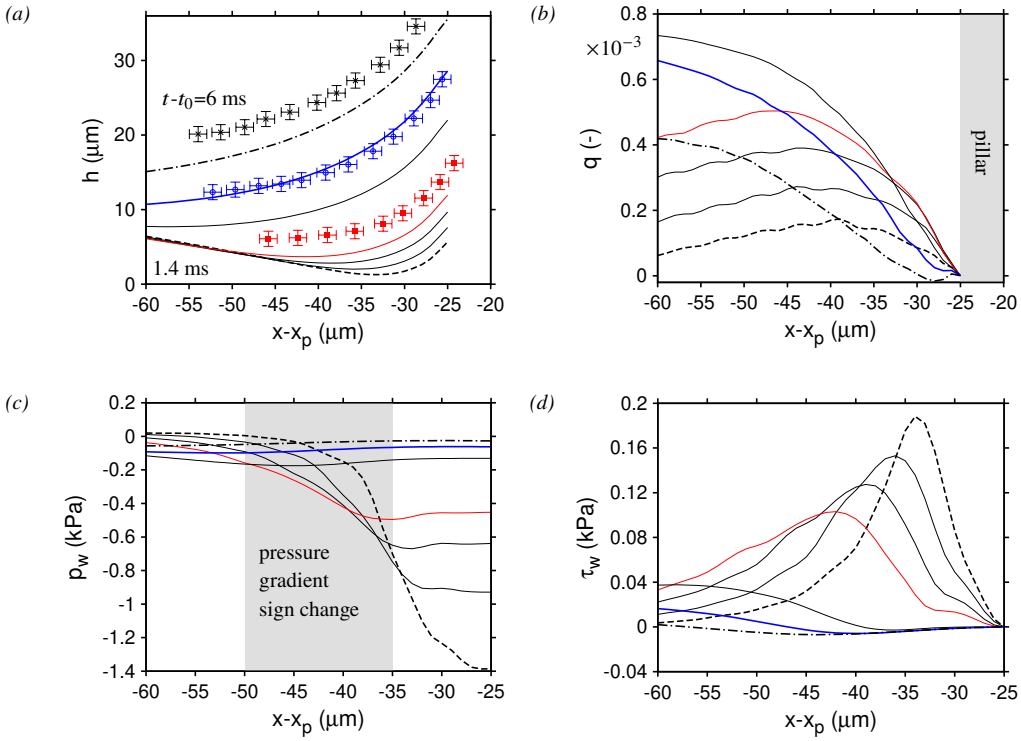


Figure 3: Time evolution of the liquid meniscus on the upstream side of the pillar ($z$=0), after initial contact at $t$=$t_0$. Curves: simulation. From dashed to dot-dashed: $t$-$t_0$=1.4, 1.6, 1.8, 2 (red), 3, 4 (blue), and 6 ms; symbols: experiments. *(a)* Film height. Red squares: $t$-$t_0$=(2 ± 1) ms, blue circles: $t$-$t_0$=(4 ± 1) ms, black crosses: $t$-$t_0$=(6 ± 1) ms; *(b)* Normalized liquid flow rate per unit width $q = \int_0^h u\,dy/(\sigma d_P/\mu)$. *(c)* Wall pressure $p_w$=$p|_{y=0}$, evidencing a change in sign of the streamwise pressure derivative. *(d)* Wall shear stress $\tau_w = \mu\partial_y u|_{y=0}$, evidencing flow reversal.

the images from our experiment in figure 1a. The frame rate of the camera being $f$=500 Hz, there is an uncertainty of ±1 ms due to a difficulty in determining the time of first contact $t_0$. With this in mind, agreement between our numerical profiles and the experimental data in figure 3a is quite good.

an uncertainty of ±1 ms due to a difficulty in determining the first contact time $t_0$

The rise of the meniscus during the early stages (1.4 ms $< t - t_0 \leq$ 2 ms) is sustained by a growing (normalized) liquid flow rate per unit width $q$=$\int_0^h u\,dy/(\sigma d_P/\mu)$

draining liquid toward the pillar (figure 3b), which is driven by a large negative wall pressure gradient $\partial_x p_w$ (dashed curve in figure 3c). This constitutes the so-called *meniscus pump* described in [18]. As shown in figure 3d, it is accompanied by a substantial variation in the wall shear stress $\tau_w$, which increases tenfold. The negative pressure gradient observed during this stage results from a strong variation of the streamwise curvature $C_{xx}$, which enters the full curvature $\kappa$ of the liquid-gas interface through:

$$\kappa = \underbrace{\frac{-\partial_{xx} h}{\left\{1 + (\partial_x h)^2\right\}^{3/2}}}_{C_{xx}} + \underbrace{\frac{-\partial_{zz} h}{\left\{1 + (\partial_x h)^2\right\}^{1/2}}}_{C_{zz}} . \tag{8}$$

However, soon after contact ($t - t_0 \geq 1.6$ ms in figure 3c), a change in sign of the pressure gradient occurs near the pillar. The resulting region of adverse pressure gradient rapidly widens and moves upstream. For $t$-$t_0$>2 ms, it covers the entire grayed region in figure 3c. As time progresses, the adverse pressure gradient causes a reduction of the liquid flow rate plotted in figure 3b (3 ms$\leq t - t_0 \leq$6 ms), and, eventually, it causes flow reversal near the bounding wall, as evidenced by the sign change of the wall shear stress profile $\tau_w(x)$ in figure 3d.

Figure 4a represents streamlines within the region of flow reversal at $t$-$t_0$=4 ms (blue curves in figures 3b, 3c, and 3d), which evidence a large separation vortex. This separation vortex constitutes the cross section of the HSV in the symmetry plane ($z$=0). Near the wall, the flow is directed away from the pillar, i.e. counter to the direction of the overall flow, and, closer to the film surface, it is directed toward the pillar. Although flow separation is often associated with inertial flows, it is also known to occur in Stokes flows over obstacles, as demonstrated by the well-known experiments of Taneda [38], reproduced in [39], as well as corresponding theoretical works [40, 41].

In the liquid film ahead of the pillar, inertia remains negligible even during

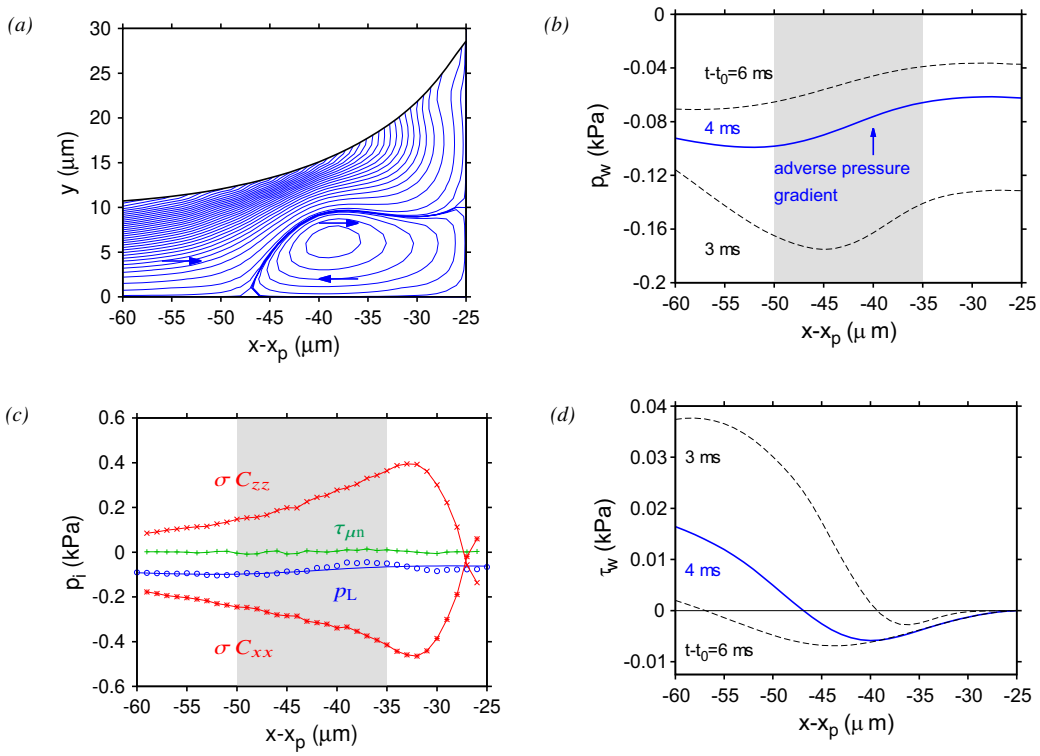


Figure 4: Mechanism of flow reversal in the symmetry plane ($z$=0) upstream of the micro-pillar. *(a)* Streamlines showing the HSV at $t - t_0 = 4$ ms. *(b)* Detail of the wall pressure profile $p_w(x)$. *(c)* Deconstruction of the adverse wall pressure gradient according to (10): $t - t_0 = 4$ ms. Solid blue: $p_w$; circles: interfacial liquid pressure $p_L$ (10); plus signs: interfacial liquid normal viscous stress $\tau_{\mu n}$ from (10); asterisks: $\sigma C_{xx}$ from (8); crosses: $\sigma C_{zz}$ from (8). *(d)* Detail of the wall shear stress profile $\tau_w(x)$.

the rapid rise of the liquid meniscus along the pillar. To demonstrate this, we introduce the directional length and velocity scales $\mathcal{L}_y$=$\underline{h}$=10 μm, $\mathcal{L}_x$=$d_p$=50 μm, and $\mathcal{U}_x$=$\underline{u}$=$2 \times 10^{-2}$ m s$^{-1}$, where $\underline{h}$ and $\underline{u}$ are representative of the film thickness and mean $x$-velocity near the leading edge of the separation vortex in figure 3a (at $t$-$t_0$=4 ms). Based on this thin-film scaling, the ratio of inertial and viscous terms in the $x$-momentum equation (2) scales as $\epsilon\underline{\mathrm{Re}}\sim 0.01$, where $\epsilon$=$\underline{h}/d_p$ denotes the length scale ratio, and $\underline{\mathrm{Re}}$=$\underline{h}\,\underline{u}/\nu$ is a rescaled Reynolds number.

Thus, the streamwise pressure derivative $\partial_x p$ is balanced by the net contribu-

tions of the streamwise viscous stress components $\tau_{xx}$=$2\mu\partial_x u$, $\tau_{yx}$=$\mu\left(\partial_y u + \partial_x v\right)$, and $\tau_{zx}$=$\mu\left(\partial_z u + \partial_x w\right)$ via:

$$0 = -\partial_x p + \mu\partial_{xx} u + \mu\partial_{yy} u + \mu\partial_{zz} u. \tag{9}$$

Near the bounding wall, the net contributions of $\tau_{xx}$ and $\tau_{zz}$ are negligible, due to the no-slip boundary condition at $y$=0, which imposes $\partial_{xx}u$=$\partial_{zz}u$=0. In this region, the pressure derivative $\partial_x p$, which is positive over a significant portion of the separation vortex, imposes a positive curvature $\partial_{yy}u$>0 on the velocity profile $u(y)$. This implies a flow direction away from the pillar, in the near-wall region. Conversely, as one moves away from the wall, $\mu\partial_{xx}u$ (and to a lesser extent $\mu\partial_{zz}u$) becomes increasingly strong and positive, which eventually leads to a change in sign of the velocity profile curvature near the liquid-gas interface, i.e. $\partial_{yy}u$<0. Assuming a stress-free interface (no dynamic effect of the gas phase), this implies a flow direction toward the pillar, near the surface of the film. Arguably, the remaining question to be answered relates to the origin of the adverse pressure gradient in our particular configuration.

In contrast to HSV forming in inertial flows [25], the origin of the adverse pressure gradient causing flow reversal in our microfluidic system (figure 4b) is not the conversion of dynamic pressure into static pressure. Variations of dynamic and hydrostatic pressure are negligible versus capillary-induced pressure variations. Based on the thin-film scaling introduced further above, the ratio of inertial and capillary terms in the $x$-momentum equation (2) scales as $\epsilon^{-2}\underline{\mathrm{We}}\sim10^{-3}$, where $\underline{We}$=$\rho\underline{u}^2\underline{h}/\sigma$ is a rescaled Weber number, and the ratio of gravitational and capillary terms as $\epsilon^{-2}\underline{\mathrm{Bo}}\sim10^{-3}$, where $\underline{\mathrm{Bo}}$=$\rho g\underline{h}^2/\sigma$ is a rescaled Bond number.

Thus, our flow is governed by a balance between viscous drag and capillarity, as suggested by the ratio of the corresponding terms in the $x$-momentum equation (2), which scales as $\epsilon^{-3}\underline{\mathrm{Ca}}\sim0.2$, where $\underline{\mathrm{Ca}}$=$\mu\underline{u}/\sigma$ denotes the capillary number. And, the adverse pressure gradient causing flow separation results from a com-

petition between variations in streamwise ($C_{xx}$) versus transverse ($C_{zz}$) curvature contributions (figure 4c), according to (8). These shape the profile of the liquid pressure at the liquid-gas interface, $p_{\mathrm{L}}(x)$, via the normal-stress inter-phase coupling condition at $y{=}h$:

$$p_{\mathrm{L}} = p_{\mathrm{G}} + \sigma\kappa + \tau_{\mu\mathrm{n}}, \tag{10}$$
$$\text{with} \quad \tau_{\mu\mathrm{n}} = \frac{2\mu}{1+(\partial_x h)^2}\left\{-\partial_x h\left(\partial_y u + \partial_x v\right) + \partial_y v + (\partial_x h)^2\,\partial_x u\right\},$$

where $p_{\mathrm{G}}$ denotes the gas pressure, which is virtually constant, $\sigma\kappa$ the pressure jump due to surface tension, and $\tau_{\mu\mathrm{n}}$ the normal liquid viscous stress (the corresponding gas stress is neglected).

In figure 4c, we have plotted different contributions to the adverse wall pressure profile at $t$-$t_0$=4 ms (blue curve in figure 4b), by making use of equation (10). We are interested in the grayed region, i.e. $-50\,\mu\mathrm{m} < x - x_p < -35\,\mu\mathrm{m}$, which corresponds to the leading portion of the separation vortex in figure 4a. First, comparing the wall pressure profile $p_{\mathrm{w}}(x)$ (solid blue curve in figure 4c) with that of the interfacial liquid pressure $p_{\mathrm{L}}(x)$ (open circles), we conclude that the wall pressure increase in this region seems to be dictated by $p_{\mathrm{L}}$, which itself is governed by the coupling condition (10). Second, the normal viscous stress $\tau_{\mu\mathrm{n}}$ in (10) (green curve with plus signs) is negligible, and thus $p_{\mathrm{L}}$ is dominated by the capillary pressure jump $\sigma\kappa$, with $\kappa{=}C_{xx}{+}C_{zz}$ (8). Third, the contribution of the transverse curvature $C_{zz}$ (red crosses) acts to produce an adverse pressure gradient ($\sigma\partial_x C_{zz}{>}0$), whereas that of the streamwise curvature $C_{xx}$ (red asterisks) acts to produce a pressure decrease toward the pillar ($\sigma\partial_x C_{xx}{<}0$). The magnitude of $C_{xx}$ and $C_{zz}$ being comparable, the competition of their spatial variations dictates the final wall pressure gradient. During the early stages, just after contact between liquid and pillar (dashed curve in figure 3a), variations in $C_{xx}$ dominate the interfacial curvature $\kappa$, but this effect gradually weakens in favor of $C_{zz}$, as the meniscus

rises along the pillar (dot-dashed curve in figure 3a). Eventually, variations in $C_{zz}$ become dominant, and this leads to the adverse pressure gradient observed in figure 3c. The increase in $C_{zz}$ toward the upstream side of the pillar observed in figure 4c results from a change in shape of the liquid-gas interface, as the flow moves toward and around the pillar, thereby espousing its cylindrical shape. Far away from the pillar, spanwise variations of the film height are weak ($\partial_{xx}h \approx 0$), and the film is virtually two-dimensional. Conversely, at the upstream-side of the pillar, the liquid-gas interface is shaped like a saddle, as a result of the streamwise curvature imposed by the liquid meniscus and the azimuthal curvature imposed by the pillar. Consequently, $\partial_{xx}h<0$ there.

To assess the mixing potential of the HSV system forming around the micro-pillar, figure 5 shows various close-up views of the flow within the liquid meniscus.We observe complex vorticity-carrying flow structures that represent a considerable intensification of spanwise and crosswise mixing within the liquid and may be exploited to enhance heat and mass transport in micro-systems. For example, the streamlines highlighted by the green/blue color palette in figure 5c evidence an effective transport of liquid from the bulk of the flow toward the wall. Moreover, the region affected by these vortical structures, i.e. the region inside the separatrix of the main HSV, is several times greater than the pillar cross section (see figure 5b). The enhancement of mixing is generated here by a simple configuration: a cylindrical pillar on an otherwise smooth substrate, without any external forcing. Thus, it is controlled entirely by the wettability of the substrate and pillar materials, as well as the pillar diameter.

## 4. Conclusion

Micro-obstacles, such as pillars or beads, when placed into the path of a liquid film spreading on a smooth substrate, are known to greatly accelerate the

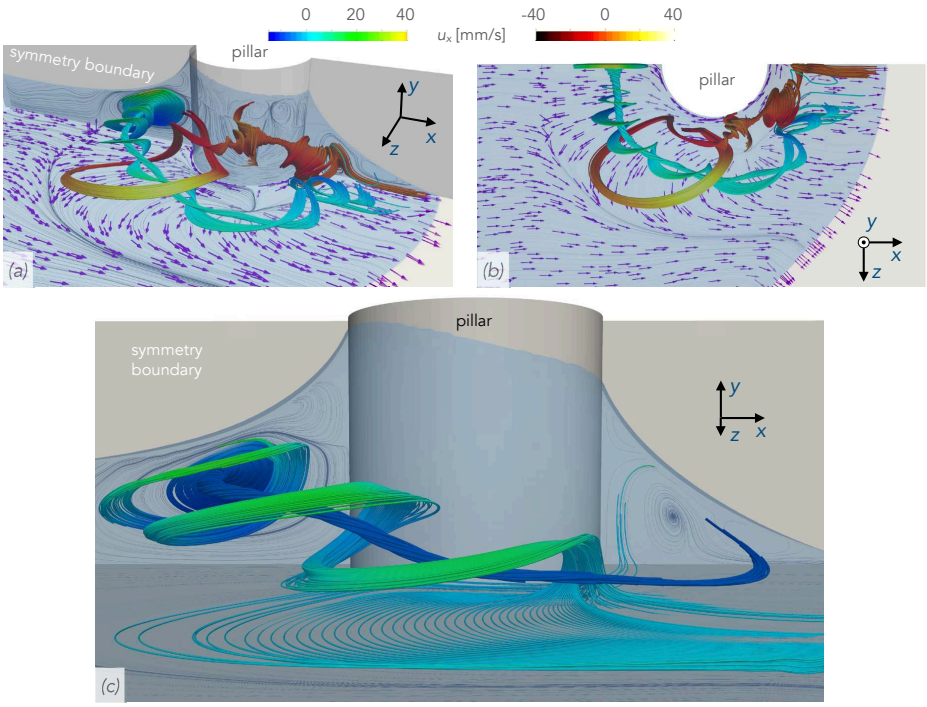


Figure 5: Mixing potential of the vortex system formed around the micro-pillar: $t - t_0$=15 ms. Colored streamlines highlight the HSV (blue/green color palette) and the wake vortex (red/yellow color palette). Wall shear stress vectors on the substrate, as well as streamlines within the symmetry plane $z = 0$ and on the pillar surface are also shown.

spreading velocity. This phenomenon, which can be exploited to enhance the wetting characteristics of materials, has been observed in various experimental and numerical studies [1, 16–19]. In the current manuscript, we have unveiled via numerical simulations another very useful feature: a complex system of vortices forming within the liquid meniscus around the micro-obstacle, which may have the potential to greatly enhance mixing. In particular, we have discovered the existence of a horseshoe vortex wrapping around the micro-pillar, which is highly untypical of low Reynolds number flows (in our system, $O(\mathrm{Re})=10^{-3}$). Hitherto, such vortices have been observed only in flows with appreciable inertia, e.g. flows around bridge pillars [20] or heat-sink pin fins [21]. By contrast, in our system, flow reversal near the wall within the horseshoe vortex is generated as a result

of surface tension forces. These cause a change in sign of the wall pressure gradient during the rise of the liquid meniscus along the pillar, as a result of the competition between the transverse and streamwise curvatures of the liquid-gas interface. Surface tension is thus responsible both for driving the liquid around the obstacle (suction toward the contact line downstream of the pillar) and for generating the adverse pressure gradient that causes flow reversal upstream of the pillar.

The micro-obstacles investigated here constitute a simple, robust, and efficient passive technique for intensifying mixing in low-Reynolds-number microfluidic systems, while improving macroscopic surface wettability. They can also produce large variations in wall shear stress during the interaction with the spreading liquid, as shown in figure 3d for our case of a cylindrical micro-pillar. This may be exploited for the cleaning of contaminated surfaces [42, 43], such as required in microprocessor technology [44] or in the food industry [45].

Based on our understanding of the mechanism underlying the capillary-driven HSV, we attempt to predict the parameter range where this phenomenon may occur. For this, we recall our thin-film length scales from section 3, i.e. $\mathcal{L}_x$ and $\mathcal{L}_y=\underline{h}$, but, this time, we make no assumption about $\mathcal{L}_x$. The length scale ratio is once again $\epsilon=\mathcal{L}_y/\mathcal{L}_x$, and we introduce $\mathcal{L}_z=d_\mathrm{p}$ for the spanwise dimension, whereas the velocity scale $\mathcal{U}_x$ will be eliminated from the problem. Firstly, dominance of capillarity versus inertia requires $\epsilon^{-2}\underline{\mathrm{We}}\sim 10^{-1}$. Secondly, balance of capillarity and viscous stresses requires $\epsilon^{-3}\underline{\mathrm{Ca}}\sim 1$. And, thirdly, competition between streamwise variations in streamwise ($C_{xx}$) and spanwise ($C_{zz}$) curvature requires $\mathcal{L}_x\sim\mathcal{L}_z$. As a result, we obtain:

$$\underline{h}\sim\left[10^{-1}d_\mathrm{p}^4\frac{\nu^2\rho}{\sigma}\right]^{\frac{1}{5}},\quad \underline{u}\sim\left[10^{-3}\frac{1}{d_\mathrm{p}^3}\frac{\nu\sigma^2}{\rho^2}\right]^{\frac{1}{5}}, \tag{11}$$

which gives estimates for the orders of magnitude of the liquid film thickness and

streamwise velocity upstream of the pillar. For our system, we obtain $\underline{h}\sim 10\,\mu\mathrm{m}$ and $\underline{u}\sim 0.1\,\mathrm{m\,s^{-1}}$ from (11), which agrees with the order of magnitude of these quantities according to our simulation data in figure 3a. The wettabilities of the substrate and the pillar are involved indirectly in (11), as they control both $\underline{h}$ and $\underline{u}$.

We conclude with a discussion to guide the design of experiments aimed at verifying the HSV discovered in our numerical simulation. The main challenge is the small characteristic size of the HSV, i.e. $l\sim 10\,\mu\mathrm{m}$. Nonetheless, micro-PIV (particle image velocimetry) or micro-PTV (particle tracking velocimetry) can be attempted using nanoparticles as tracers. For example, we expect pathlines of particles traveling near the substrate to exhibit a much stronger deflection around the pillar than its geometrical size would imply, as a result of the separatrix enveloping the pillar foot. Promising preliminary experiments using the setup from figure 1a are currently under way and will be the subject of future work.


## Acknowledgment

This work was supported by the Grant-in-Aid for Scientific Research (B) (grant number: 19H02083) from the Japan Society for the Promotion of Science (JSPS). This work also benefited from the support of the project FEFS ANR-CE21-2018 of the French National Research Agency (ANR), from the Suzuki Foundation, and from the Tokyo University of Science Grant for International Joint Research.


## Declaration of Competing interest

The authors report no conflict of interest.

## Author contributions

K.O. and H.N. contributed equally to this work. G.F.D., H.N.Y., F.Z. and I.U. designed research; K.O. and H.N. performed simulation; K.O., H.N., G.F.D., H.N.Y., F.Z., K.K., L.M. and I.U. analyzed data; G.F.D., H.N.Y., F.Z. and I.U. wrote the paper.

## References


[1] L. Mu, D. Kondo, M. Inoue, T. Kaneko, H. N. Yoshikawa, F. Zoueshtiagh, I. Ueno, Sharp acceleration of a macroscopic contact line induced by a particle, Journal of Fluid Mechanics 830 (2017) R1.

[2] H. A. Stone, A. D. Strook, A. Ajdari, Engineering flows in small devices: Microfluidics toward a lab-on-a-chip, Annu. Rev. Fluid Mech. 36 (2004) 381–411.

[3] W.-Y. Huang, C.-A. Liu, R.-S. Fan, Z.-D. Lin, K. Wang, G.-B. Lee, Automatic optimization of drug cocktails on an integrated microfluidic system, Biomicrofluidics 11 (3) (2017) 034109.

[4] A. W. Browne, C. H. Ahn, An in-line microfluidic blood sampling interface between patients and saline infusion systems, Biomedical Microdevices 13 (4) (2011) 661–669.

[5] C. C. Tseng, R. J. Yang, W. J. Ju, L.-M. Fu, 2018, Microfluidic paper-based platform for whole blood creatinine detection, Chemical Engineering Journal 348 (2018) 117–124.

[6] C. Colosi, S. R. Shin, V. Manoharan, S. Massa, M. Costantini, A. Barbetta, M. R. Dokmeci, M. Dentini, A. Khademhosseini, Microfluidic Bioprinting of

Heterogeneous 3D Tissue Constructs Using Low-Viscosity Bioink, Advanced Materials 28 (4) (2016) 677–684.

[7] S. Alagoz, Y. Apak, Removal of spoiling materials from solar panel surfaces by applying surface acoustic waves, Journal of Cleaner Production 253 (2020) 119992.

[8] K. Ward, Z. H. Fan, Mixing in microfluidic devices and enhancement methods, Journal of Micromechanics and Microengineering 25 (9) (2015) 094001–18.

[9] C.-Y. Lee, C.-L. Chang, Y.-N. Wang, L.-M. Fu, Microfluidic Mixing: A Review, International Journal of Molecular Sciences 12 (2011) 3263–3287.

[10] A. D. Stroock, S. K. W. Dertinger, A. Ajdari, I. Mezic, H. A. Stone, G. M. Whitesides, Chaotic mixer for microchannels, Science 295 (5555) (2002) 647–651.

[11] X. Hu, Z. Wang, D. J. Hwang, C. E. Colosqui, T. Cubaud, Viscous liquid–liquid wetting and dewetting of textured surfaces, Soft Matter 17 (2021) 879–886. doi:10.1039/D0SM01524E.

[12] V. Kumaran, Stability and the transition to turbulence in the flow through conduits with compliant walls, Journal of Fluid Mechanics 924 (2021) P1. doi:10.1017/jfm.2021.602.

[13] C. J. Baker, The laminar horseshoe vortex, Journal of Fluid Mechanics 95 (2) (1979) 347–367.

[14] J. Bico, C. Tordeux, D. Quéré, Rough wetting, Europhysics Letters 55 (2) (2001) 214–220.

[15] B. Darbois-Texier, P. Laurent, S. Stoukatch, S. Dorbolo, Wicking through a confined micropillar array, Microfluidics and Nanofluidics 20 (4) (2016) 53.

[16] L. Mu, H. N. Yoshikawa, D. Kondo, T.Ogawa, M. Kiriki, F. Zoueshtiagh, M. Motosuke, T. Kaneko, I. Ueno, Control of local wetting by microscopic particles, Colloids and Surfaces A 555 (2018) 615–620.

[17] L. Mu, H. N. Yoshikawa, F. Zoueshtiagh, T. Ogawa, M. Motosuke, I. Ueno, Quick liquid propagation on a linear array of micropillars, Langmuir 35 (2019) 9139–9145.

[18] H. Nakamura, T. Ogawa, M. Inoue, T. Hori, L. Mu, H. N. Yoshikawa, F. Zoueshtiagh, G. Dietze, T. Tsukahara, I. Ueno, Pumping effect of heterogeneous meniscus formed around spherical particle, Journal of Colloid and Interface Science 562 (2020) 133–141.

[19] H. Nakamura, V. Delafosse, G. F. Dietze, H. N. Yoshikawa, F. Zoueshtiagh, L. Mu, I. Ueno, Enhancement of meniscus pump by multiple particles, Langmuir 36 (2020) 4447–4453.

[20] A. H. Gazi, M. S. Afzal, A review on hydrodynamics of horseshoe vortex at a vertical cylinder mounted on a flat bed and its implication to scour at a cylinder, Acta Geophysica 68 (2020) 861–875. doi:10.1007/s11600-020-00439-810.1007/s11600-020-00439-8.

[21] C. D. Anderson, S. P. Lynch, Time-resolved stereo piv measurements of the horseshoe vortex system at multiple locations in a low-aspect-ratio pin-fin array, Experiments in Fluids 57 (2016) 5.

[22] R. L. Simpson, Junction flows, Annual Review of Fluid Mechanics 33 (2001) 415–443.

[23] C. Lin, T. C. Ho, S. Dey, Characteristics of steady horseshoe vortex system near junction of square cylinder and base plate, Journal of Engineering Mechanics 134 (2) (2008) 184–197.

[24] S. M. Hajimirzaie, A. G. Tsakiris, J. H. J. Buchholz, A. N. Papanicolaou, Flow characteristics around a wall-mounted spherical obstacle in a thin boundary layer, Experiments in Fluids 55 (2014) 1762.

[25] G. Launay, E. Mignot, N. Riviere, R. Perkins, An experimental investigation of the laminar horseshoe vortex around an emerging obstacle, Journal of Fluid Mechanics 830 (2017) 257–299.

[26] S. S. Deshpande, L. Anumolu, M. F. Trujillo, Evaluating the performance of the two-phase flow solver interfoam, Computational science & discovery 5 (1) (2012) 014016.

[27] C. W. Hirt, B. D. Nichols, Volume of fluid (VOF) method for the dynamics of free boundaries, Journal of Computational Physics 39 (1981) 201–225.

[28] J. U. Brackbill, D. B. Kothe, C. Zemach, A continuum method for modeling surface tension, Journal of Computational Physics 100 (2) (1992) 335–354.

[29] D. Gründing, M. Smuda, T. Antritter, M. Fricke, D. Rettenmaier, F. Kummer, P. Stephan, H. Marschall, D. Bothe, A comparative study of transient capillary rise using direct numerical simulations, Applied Mathematical Modelling 86 (2020) 142–165.

[30] A. Prosperetti, G. Tryggvason (Eds.), Computational Methods for Multiphase Flow, Cambridge University Press, 2007.

[31] D. L. Youngs, Numerical Methods for Fluid Dynamics, Academic Press,

New York, 1982, Ch. Time-dependent multi-material flow with large fluid distortion, pp. 273–285.

[32] M. Sussman, E. G. Puckett, A coupled level set and volume-of-fluid method for computing 3d and axisymmetric incompressible two-phase flows, Journal of Computational Physics 162 (2) (2000) 301–337.

[33] A. A. Saha, S. K. Mitra, Effect of dynamic contact angle in a volume of fluid (vof) model for a microfluidic capillary flow, Journal of Colloid and Interface Science 339 (2) (2009) 461–480.

[34] J. Q. Feng, A computational study of high-speed microdroplet impact onto a smooth solid surface, Journal of Applied Fluid Mechanics 10 (1) (2017) 243–256. doi:10.18869/acadpub.jafm.73.238.26440.

[35] S. G. Mallinson, T. J. Barber, G. H. Yeoh, G. D. McBain, Simulation of droplet impact and spreading using a simple dynamic contact angle model, in: T. C. W. Lau, R. M. Kelso (Eds.), Proceedings of the 21st Australasian Fluid Mechanics Conference, Australasian Fluid Mechanics Society, Adelaide, 2018.

[36] L. H. Tanner, The spreading of silicone oil drops on horizontal surfaces, Journal of Physics D 12 (1979) 1474–1484.

[37] J. Snoeijer, B. Andreotti, Moving contact lines: Scales, regimes, and dynamical transitions, Annual Review of Fluid Mechanics 45 (2013) 269–292.

[38] S. Taneda, Visualization of separating Stokes flows, Journal of the Physical Society of Japan 46 (6) (1979) 1935–1942.

[39] M. Van Dyke, An album of fluid motion, Vol. 176, Parabolic Press Stanford, 1982.

[40] J. M. Dorrepaal, M. E. O'Neill, K. B. Ranger, Axisymmetric stokes flow past a spherical cap, Journal of Fluid Mechanics 75 (2) (1976) 273–286.

[41] A. M. J. Davis, M. E. O'Neill, Separation in a slow linear shear flow past a cylinder and a plane, Journal of Fluid Mechanics 81 (3) (1977) 551–564.

[42] S. Khodaparast, M. K. Kim, J. E. Silpe, H. A. Stone, Bubble-driven detachment of bacteria from confined microgeometries, Environmental Science & Technology 51 (3) (2017) 1340–1347. doi:10.1021/acs.est.6b04369.

[43] F. Zoueshtiagh, M. Baudoin, D. Guerrin, Capillary tube wetting induced by particles: towards armoured bubbles tailoring, Soft Matter 10 (2014) 9403–9412. doi:10.1039/C4SM01648C.

[44] H. F. Okorn-Schmidt, F. Holsteyns, A. Lippert, D. Mui, M. Kawaguchi, C. Lechner, P. E. Frommhold, T. Nowak, F. Reuter, M. B. Piqué, C. Cairos, R. Mettin, Particle cleaning technologies to meet advanced semiconductor device process requirements, ECS Journal of Solid State Science and Technology 3 (1) (2014) N3069–N3080.

[45] J. M. Vicaria, E. Jurado-Alameda, O. Herrera-Márquez, V. Olivares-Arias, A. Ávila-Sierra, Analysis of different protocols for the cleaning of corn starch adhering to stainless steel, Journal of Cleaner Production 168 (2017) 87–96.